

Article

Pixel Tracking for Micro-Motion Estimation of Maritime Targets by COSMO-SkyMed Synthetic Aperture Radar Data - An Operative Assessment

Biondi Filippo ^{1,†,‡} 

¹ University of L'Aquila; biopippoo@gmail.com

* Correspondence: biopippoo@gmail.com; Tel.: +39-335-833-4216

† Current address: Via Luca Benincasa 21/B 06073 Corciano Perugia (Italy)

‡ These authors contributed equally to this work.

Version May 20, 2019 submitted to Journal Not Specified

Abstract: This research aims to estimate the micro-motion (m-m) of ships. The problem of motion and m-m detection of targets is usually solved using synthetic aperture radar (SAR) along-track interferometry (ATI) which is observed employing two radars spatially distanced by a baseline extended in the azimuth direction. This paper is proposing a new approach where the m-m estimation of ships, occupying thousands of pixels, is measured processing the information given by sub-pixel tracking generated during the coregistration process of several re-synthesized time-domain and overlapped sub-apertures. The SAR products are generated splitting the raw data, according to a small-temporal baseline strategy, observed by one single wide-band staring spotlight (ST) SAR image. The predominant vibrational modes of different ships are estimated and results are promising to extend this application in performing surveillance also of land-based industries activities. Experiments are performed processing one ST SAR image observed by the COSMO-SkyMed satellite system.

Keywords: Synthetic aperture radar (SAR), along-track interferometry (ATI), sub-pixel offset tracking (sPOT), COSMO-SkyMed (CSK), staring spotlight (ST), micro-motion (m-m), vibrations, frequency modes.

1. Introduction

Synthetic aperture radar (SAR) provides high-resolution images of static ground scenes, whereas processing of data containing ground object motion results in varying focusing effects. A special case of such motion is vibration where its pattern may be distinctly recognizable in focused SAR intensity images as well as in a precise amplitude analysis. The X-band SAR can be well suited to image vibration because its wavelength is close to typical vibration amplitudes. This work extends the investigation technique observed in [1] where the pixel tracking has been used for the first time to detect small movements in space of marine targets. Before this work, several interesting research has been performed in the field of micro-motion (m-m) estimation. In [2] the effects of rotation and vibration in millimeter-waveforms SAR processing simulated and real data has been assessed. Vibrating targets cause the modulation of the azimuth phase history of a SAR image. This phenomenon may be considered as a time-dependent micro-Doppler (m-D) frequency. In [3] the oscillation frequency and amplitude were calculated from the time-frequency distributions and the results agreed with available ground truths. In [4] a vibrating m-D signature for a Bistatic SAR system with a fixed receiver was analyzed and compared to the signature obtained in a monostatic SAR system. The m-D effect was derived for a vibrating target in the bistatic SAR. The derived model was useful for m-D classification and suitable to perform target recognition. Simulations for 94 GHz and 10 GHz

33 has been given and the results confirmed the derived model. Research [5] implemented a wavelet
 34 approach for providing the m-m analysis of inverse SAR (ISAR) systems. Future extraction has been
 35 successfully applied to SAR data scene collected by military and civilian radars. In [6] a detector based
 36 on the generalized likelihood ratio test (GLRT) has been proposed to detect targets m-m. The detection
 37 performance demonstrated by both simulated and quasi-real data, showing favorable detection ability
 38 under low signal-to-noise/clutter ratios. Some times the m-D effect may significantly decrease the
 39 readability of the ISAR and SAR images. Research [7] successfully designed a method to remove
 40 these effects based on the spectrogram and complex time-frequency analysis of raw data. Research
 41 [8] designed the vibration signal modeling of vibrating targets using multiple input multiple output
 42 (MIMO) SAR systems. Simulations verified the influence of vibration parameters on imaging and
 43 time-frequency profile and showed the m-D signature difference through different MIMO channels.
 44 The results demonstrate also the potential of MIMO SAR for 3D m-m estimation. In [9], [10], [11], and
 45 [12] different strategies for ships and ship wake detection has been consolidated using also Compresses
 46 Sensing and low-rank plus sparse decomposition implemented by convex-programming approaches.
 47 Several methods has been implemented in [13], [14], and [15] for Earth displacement estimation
 48 tracking only the magnitude of single-look-complex (SLC) couples of interferometric SAR images.
 49 This procedure is evaluated by the coregistration computational process where the azimuth and range
 50 shifts are used to build-up a two-dimensional displacement map. In this paper, the author used this
 51 method for estimating the m-D produced on maritime targets using several temporal sub-apertures of
 52 a single COSMO-SkyMed staring-spotlight (ST) SAR image. Results showed the possibility to estimate
 53 the vibrational fingerprint of the maritime vessel which results are promising to extend this work in
 54 performing surveillance also on land-based industries facilities.

55 The remainder of this paper is organized as follows. The details of the estimation procedure are
 56 described in Section 2. This section is divided into subsection 2.1 devoted to describing the technique
 57 used to estimate the coregistration shifts and subsection 2.2 devoted to providing a detailed description
 58 of the computational architecture designed to estimate the m-m. Section 3 contains the illustrative
 59 examples based upon two real study-cases data, while subsection 3.1 gives a detailed explanation of
 60 the results estimated on the case of study one and subsection 3.2 is devoted to giving results concerning
 61 the case of study two. The last section (Section 4) concludes the paper and introduces future research
 62 in the area.

Table 1. SAR acquisition characteristics summary

Parameter	Value
Near Incidence Angle	47.3°
Far Incidence Angle	46.9°
Range Focusing Bandwidth	250 MHz
Azimuth Focusing Bandwidth	25 kHz
Orbit height	600km
Chirp central frequency	9.6 GHz
Minimum points for each tile	50
Acquisition time	01 June 2014
Acquisition location	Taranto (Italy)

Table 2. Coregistration parameters

Parameter	Value
Initial shifts	Coarse XCorro
Number of points	4000
Correlation threshold	0.8
Oversampling factor	128
shearch pixel window	48x48 pixel
Points skimming (minimum points)	30
Use of DEM	No
Doppler Centr. Est. Strategy	Polynomials

63 2. Estimation Procedure and computational scheme

64 2.1. Estimation procedure

65 Sub-pixel offset tracking (sPOT) is a relevant technique to measure large-scale ground
66 displacements in both range and azimuth directions. The technique is complementary to differential
67 interferometric SAR (DInSAR) and persistent scatterers interferometry (PSInSAR) when the radar
68 phase information is unstable. In this work, the author estimates the offset fields which are generated
69 with a normalized cross-correlation of image patches of detected real-valued SAR intensity images. The
70 successful estimation of a reliable two-dimensional local image offsets field depends on the presence
71 of nearly identical features in the multi-temporal SAR images stack under test. This technique is based
72 principally on the maximization of the normalized cross-correlation existing between two couples of
73 registered SAR intensity image patches. In order to give an operative start-up of this sPOT estimation,
74 the author used the software SARPROZ [16]-[17] developed by Prof. D. Perissin in order to process the
75 temporal SAR sub-apertures. The accuracy of this sPOT method depends on the coregistration settings
76 parameters and the topographic relief. For this work, the author set the cross-correlation window size
77 at 128×128 pixels and the oversampling factor at 64 in both the range and azimuth directions. All the
78 coregistration parameters are reported in Table 2. The offset components of the sub-pixel normalized
79 cross-correlation, according to [18]-[19] is described by the complex parameter D_{tot} (range, azimuth)
80 which is estimated by the following equation:

$$D_{\text{tot}}(\text{range, azimuth}) = D_{\text{displ}} + D_{\text{topo}} + \quad (1)$$

$$+ D_{\text{orbit}} + D_{\text{control}} + D_{\text{atmosphere}} + D_{\text{noise}}$$

81 In (1) the parameter D_{displ} is the offset component generated by the earth displacement, the parameter
82 D_{topo} is the offset component generated by the earth displacement when located on highly sloped
83 terrain, the parameter D_{orbit} is the offset caused by residual errors of the satellite orbits, The parameter
84 D_{control} is the offset component generated by general attitude and control errors of the flying satellite
85 trajectory. The last two parameters $D_{\text{atmosphere}}$ and D_{noise} are the contributions generated by the
86 electromagnetic aberrations due to atmosphere parameters space and time variations and general
87 disturbances due to thermal and quantization noise. The atmospheric time-variation during the very
88 short time interval of this SAR image acquisition has little influence on the temporal component of
89 the last displacement parameters because of its low accuracy. All errors are compensated choosing
90 only high energy and stable points and subtracting the initial offsets in order to retrieve the shifts
91 contributions only generated by the target displacement.

92 2.2. Computational Scheme Description

93 This subsection will describe the functionalities of the calculation architecture used to estimate
94 the m-m. The computational schema is visible in Figure 1 (a). The input of the system is constituted
95 of a single raw data constituting block 1. The computational block 2 is constituted by a temporal

n-stage splitter that has the task to produce n temporal sub-apertures. In this project, we have chosen to generate 31 sub-products. The computational stage 3 has instead the computation to focus all the n sub-apertures. The final products are a time series of SAR images in the SLC configuration with a lower resolution in azimuth, inversely proportional to the amount of lost Doppler band. SAR products generated by block 3 are not yet coregistered, this feature is implemented by computational block number 5. This stage performs the sub-pixel coregistration for which the setting parameters are generated by block 4. The coregistration settings are shown in Tabs. 2. It is considered important to describe the strategy for choosing the master of the multiple co-registration processes. The coregistration strategy is "Small-temporal baseline" with the sliding master. The output of the co-recorder is represented by block 6. The result is a stack of maps of shifts in range and azimuth. At this point, the computational blocks 7 and 8 perform pixel by pixel analysis to estimate the oscillations of the ships. Figure 1 (b) represents a more detailed explanation of computational blocks 7 and 8. The input of block 7 consists of a single column of shifts where in this case it has a dimensionality of $1 \times 31 \in \mathbb{C}$. The vector of shifts is complex in that below the coregistration process the displacements are estimated both in the range direction and in the azimuth direction. The computational block 7.1 has the function of interpolating the input data by a factor of 5. Subsequently, the block 7.2 carries out the operation of fast Fourier transform (FFT) in order to calculate the modes of oscillation on the slant coordinates identified by the pixel of the original image focused in full band. Computational block 8 performs the m-m extrapolation which is composed by a bank of bandpass filters in order to extrapolate the oscillations in the time domain. The outputs are observed in the frequency domain by the signal $u(f)$ and in the time domain by the signal $u(t)$.

3. Experimental Results

This section is designed to give a detailed description of the experimental results. The work was carried out by analyzing the vibrational modes of two study cases concerning two ships at anchor. It was also decided to analyze in depth the frequency response and the trend over time of the vibrations by selecting seven measurement points concerning the case of study one and two measurement points on the case of study two. All points were distributed widely on the outer deck of the ships. The results also include the estimation of the distribution of the resonance frequencies distributed in the space where a comparative analysis of two vibration profiles extracted both along the keel and along the ship's deck was also carried out.

3.1. Study Case Number One Results

Figure 2 shows the ST-SAR acquisition geometry. The SAR observation lasted about 12 seconds using approximately 25 kHz of Doppler band. The whole image formation history was divided into 31 temporal azimuth sub-apertures lasting about 0.3871s, according to a small temporal baselines strategy. Figure 3 (a) depicts the magnitude of the ROI of the ship under test. Figure 3 (b) represent the estimated vibration energy integrated through time. and Figure 4 (a) is the average phase spanned in time of the pixel displacement. Figure 4 (b) depicts the measurement points map of the ship. In this case study, 7 measurement points were considered where for each of them the vibration spectrum and the temporal trend of movements in the time domain were measured. The first measurement point (in number 1) was located on the bow of the ship. measurement point number 2 was located in the center of the ship on the left side. measurement point number 3 was chosen on the position standing near the sterncastle, the Command bridge area. Measurement point 4 has been located at the end of the stern main mast, while point 5 is located on the straight side of the sterncastle. Point 6 is located near the dashboard on the straight side and lastly, point 7 has been chosen to be located near the center of the ship on the forward side. Figure 5 (a) represents the trend over time of the vibrations existing at measurement point number 1. The amplitude of the vibrations are of a medium entity in fact, as shown by Figure 3 (b), at this point coincides average energy equal to -5dB. The vibrational modes, shown in Figure 5 (b), are very intense where the maximum in terms of spectral amplitude has been

144 localized at about 37 Hz. The results for measurement point number 2 are shown in Figures 6 (a) and
145 6 (b). Figure 6 (a) shows the trend of displacements over time. On this second measurement point,
146 the amplitude of oscillation is rather low compared to the previous case where the maximum is equal
147 to 0.3. Figure 6 (b) shows the vibrational frequency spectrum. In this case, the spectral lines are well
148 defined with a maximum allocated at about 34 Hz. The average amplitude of the vibrations is around
149 0.4, while the spectrum clearly shows energy accumulations on the frequencies allocated around 23
150 Hz and 38 Hz. The results for measurement point number 3 are shown in Figures 7 (a) and 7 (b).
151 Figure 7 (a) shows the trend of displacements over time. On this measurement point, the amplitude of
152 oscillation is also lower with respect to vibrations observed on the measurement point 1 where the
153 maximum is equal to 0.25. Figure 7 (b) shows the vibrational frequency spectrum. In this case, the
154 spectral lines are well defined with a maximum allocated at about 34 Hz. The average amplitude of the
155 vibrations at higher frequencies is around 0.2, while the spectrum clearly shows energy accumulations
156 on the frequencies allocated approximately around 23 Hz and 36 Hz. The measurement point number
157 4 is the most particular because it was chosen to study the vibrations present at the end of the front
158 master of the ship. As Figure 8 (a) shows, the oscillations over time have numerous peaks at the
159 maximum amplitude of 1. The preponderance of these peaks is very stable at 25 Hz, as shown by
160 Figure 8 (b), which represents the spectrum. The results concerning the time domain vibration pattern
161 of measurement points 5 and 6 have been reported in Figures 9 (a) and 10 (a) respectively. The figures
162 show a similarity with mean values around 0.4. The spectra are shown in Figures 9 (b) and 10 (b),
163 confirming resonance oscillations of around 12 and 42 Hz for point 5 and 32 Hz at the measurement
164 point 6. No significant oscillations were measured at this point. Figure 11 (a) shows the time course of
165 the displacement observed on the measurement point number 7 for which negligible amplitude values
166 are measured (on average about 0.0030 compared to the maximum of 1). The spectrum has a very low
167 maximum frequency, allocated around 2 Hz (result showed in Figure 11 (b)). A global view of the
168 resonance frequencies distributed over all the pixels composing the ship is shown in Figure 12. The
169 figure shows two reflectivity profiles marked with the numbers 1 and 2. The first reflectivity profile
170 is shown in Figure 13 (a). This orientation was chosen in order to study the trend of keel vibrations.
171 This representation in amplitude is given by the plus markers while the frequency value is represented
172 by times markers. It is considered very important to underline that both physical values have been
173 normalized to 1 so as to show the trend on the same graph. Figure 13 (b) finally represents the trend of
174 the resonance frequency (plus points) to the vibration energy (times symbols). The observations are
175 measured along with the vibrational profile 2. It was found that an increase in frequency corresponds
176 to an increase in vibration energy, both on the keel (profile number 1) and on the transverse profile
177 (profile number 2).

178 3.2. Study Case Number Two Results

179 The second case study is the study of a second ship for which the visible vibrational modes have
180 been calculated, also in this case, in the time and frequency domain. For this second case, it was
181 decided to process data by observing a merchant ship specially chosen with many lateral lobes and
182 disturbances due to defocusing effects that are markedly more visible in the Doppler domain. This
183 worst case was chosen in order to test the robustness of the movement estimation algorithm. Figure
184 14 is the SLC in the magnitude of the ship. The optical image of the vessel concerning the second
185 case study is depicted in Figure 15 (a). On this case study, there are two measurement points, the
186 measurement point number 1 is located on top of the funnel and the second measurement point is
187 located on the first crane of the ship. Figure 15 (b) represents the energy map of vibrations where a
188 high energy level can be seen at the measurement point 1 and coinciding with the chimney stack. This
189 infrastructure clearly vibrates more than the rest of the ship and this anomaly is correctly detected.
190 Figure 16 (a) represents the vibration spectrum at the measurement point 1 where the predominant
191 modes of vibration in the form of spectral lines are very visible. Some predominant frequencies are
192 detected at approximately 36 Hz. The time domain of the vibrational point 1 is depicted in Fig. 15 (b).

193 Figure 16 (a) is the vibration spectrum of measurement point 2 where other predominant vibration
194 modes in the form of some spectral lines are very visible. Other predominant frequencies are detected
195 at approximately 38 Hz. The time domain of the vibrational point 2 is depicted in Fig. 16 (b).

196 4. Discussion and future assessments

197 The results obtained in this research work have shown that the use of amplitude information alone
198 is sufficient statistics to estimate the m-m generated by ships. SAR technology is projected to observe
199 environments with increasing resolution. This feature will lead the scientific community to develop
200 increasingly precise signal processing algorithms. The choice of processing high-resolution SAR
201 Spotlight data was therefore aimed at the possibility of obtaining displacement maps with millimetric
202 precision to obtain the estimate of m-m. The results of this work open the door to the possibility of
203 increasing the detection performance and especially the recognition of marine targets. The possibility
204 of estimating the vibrational map of coded targets allows, for example, to recognize if a ship has or
205 has not started and operational engines, or allows to locate the position of the engine room within
206 the naval silhouette. Finally, it could be recognized in number and type of engines installed on board,
207 through the implementation of special deep-learning algorithms. At the moment, through this research
208 work, the author has been able to estimate the vibrations in the time and frequency domain on the said
209 positions in the space occupied by two different ships. Considering the vibrations observed in the time
210 domain, the energy was estimated and, with regard to the frequency study, it was possible to observe
211 the main modes of oscillation. It is very likely that the vibrational modes of the machines used to
212 generate the electrical energy on board were observed, and therefore the oscillations generated by the
213 Diesel alternators. Future efforts will be devoted to the estimation of vibrations generated by terrestrial
214 industrial installations and for the generation of electricity such as coal-fired and nuclear power plants.
215 The proposed technique appears to have immediate and promising operational applications.

216 5. Conclusions

217 This research aimed to estimate the m-m of ships. This paper is proposed a new approach where
218 the m-m estimation of ships, occupying thousands of pixels, is measured processing the information
219 given by sub-pixel tracking generated during the coregistration process of several re-synthesized
220 time-domain and not-overlapped sub-apertures. The SAR products was generated splitting the raw
221 data, according to a small-temporal baseline strategy, observed by one single wide-band ST SAR image.
222 The predominant vibrational modes of different ships has been estimated and results are promising to
223 extend this application in performing surveillance also of land based industries activities. Experiments
224 where performed processing one ST SAR image observed by the CSK satellite system.

225 6. Materials and Methods

226 In this section will be described the all materials used and the methods which has been applied
227 and useful for replicating the experiments. The author used a laptop configured with a core i7 and 16
228 GB RAM. The author used the software SARPROZ: <https://www.sarproz.com/>. This software has a
229 too, that is able to estimate the coregistration shifts. The author used also MATLAB, using his own
230 codes to generate the Doppler sub-apertures.

231 **Conflicts of Interest:** The author declare no conflict of interest. The author whose names is listed immediately
232 below the tittle certify that they have NO affiliations with or involvement in any organization or entity with
233 any financial interest (such as honoraria; educational grants; participation in speakers' bureaus; membership,
234 employment, consultancies, stock ownership, or other equity interest; and expert testimony or patent-licensing
235 arrangements), or non-financial interest (such as personal or professional relationships, affiliations, knowledge
236 or beliefs) in the subject matter or materials discussed in this manuscript. No founders are involved during the
237 designation and the life of this projects.

238 Abbreviations

239 The following abbreviations are used in this manuscript:

240

SS	Staring Spotlight
micro-motion	m-m
ROI	Region of Interest
MTI	Moving Target Indicator
LRSD	Low-Rank plus Sparse Decomposition
RT	Radon transform
MIMO	Multiple Input Multiple Output
sPOT	Pixel Offset Tracking
241 GLRT	Generalized Likelihood Ratio Test
LOS	Line of Sight
ERS	European remote sensing satellite system
CSK	COSMO-SkyMed
ATI	Along-Track-Interferometry
SAR	Synthetic Aperture Radar
InSAR	Interferometric SAR
PSInSAR	Persistent Scatterers Interferometric SAR

242 References

- 243 1. Filippo, Biondi. "COSMO-SkyMed Staring Spotlight SAR Data for Micro-Motion and Inclination Angle
244 Estimation of Ships by Pixel Tracking and Convex Optimization." *Rem. Sens.* 11.7 (2019): 766.
- 245 2. Ruegg, Maurice, Erich Meier, and Daniel Nuesch. "Vibration and rotation in millimeter-wave SAR." *IEEE
246 Transactions on Geoscience and Remote Sensing* 45.2 (2007): 293-304.
- 247 3. Sparr, Trygve, and Bard Krane. "Micro-Doppler analysis of vibrating targets in SAR." *IEE
248 Proceedings-Radar, Sonar and Navigation* 150.4 (2003): 277-283.
- 249 4. Clemente, Carmine, and John J. Soraghan. "Vibrating target micro-Doppler signature in bistatic SAR with a
250 fixed receiver." *IEEE Transactions on Geoscience and Remote Sensing* 50.8 (2012): 3219-3227.
- 251 5. Thayaparan, T., et al. "Micro-Doppler analysis of a rotating target in synthetic aperture radar." *IET Signal
252 Processing* 4.3 (2010): 245-255.
- 253 6. Deng, B., et al. "Generalised likelihood ratio test detector for micro-motion targets in synthetic aperture
254 radar raw signals." *IET Radar, Sonar Navigation* 5.5 (2011): 528-535.
- 255 7. Stankovic, Ljubisa, et al. "Micro-Doppler removal in the radar imaging analysis." *IEEE Transactions on
256 Aerospace and Electronic Systems* 49.2 (2013): 1234-1250.
- 257 8. Zhao, Guanhua, et al. "Imaging and micro-Doppler analysis of vibrating target in multi-input?multi-output
258 synthetic aperture radar." *IET Radar, Sonar Navigation* 9.9 (2015): 1360-1365.
- 259 9. Bandiera, Francesco, Danilo Orlando, and Giuseppe Ricci. "On the CFAR property of GLRT-based direction
260 detectors." *IEEE transactions on signal processing* 55.8 (2007): 4312-4315.
- 261 10. F. Biondi, "Low rank plus sparse decomposition of synthetic aperture radar data for maritime surveillance,"
262 2016 4th International Workshop on Compressed Sensing Theory and its Applications to Radar, Sonar and
263 Remote Sensing (CoSeRa), Aachen, 2016, pp. 75-79.
- 264 11. BIONDI, Filippo. Low-rank plus sparse decomposition and localized radon transform for ship-wake
265 detection in synthetic aperture radar images. *IEEE Geosc. and Rem. Sens. Letters*, 2018, 15.1: 117-121.
- 266 12. Biondi, Filippo. "A Polarimetric Extension of Low-Rank Plus Sparse Decomposition and Radon Transform
267 for Ship Wake Detection in Synthetic Aperture Radar Images." *IEEE Geoscience and Remote Sensing Letters*
268 16.1 (2019): 75-79.
- 269 13. Casu, Francesco, et al. "Deformation time-series generation in areas characterized by large displacement
270 dynamics: The SAR amplitude pixel-offset SBAS technique." *IEEE Transactions on Geoscience and Remote
271 Sensing* 49.7 (2011): 2752-2763.
- 272 14. Scambos, Theodore A., et al. "Application of image cross-correlation to the measurement of glacier velocity
273 using satellite image data." *Remote sensing of environment* 42.3 (1992): 177-186.

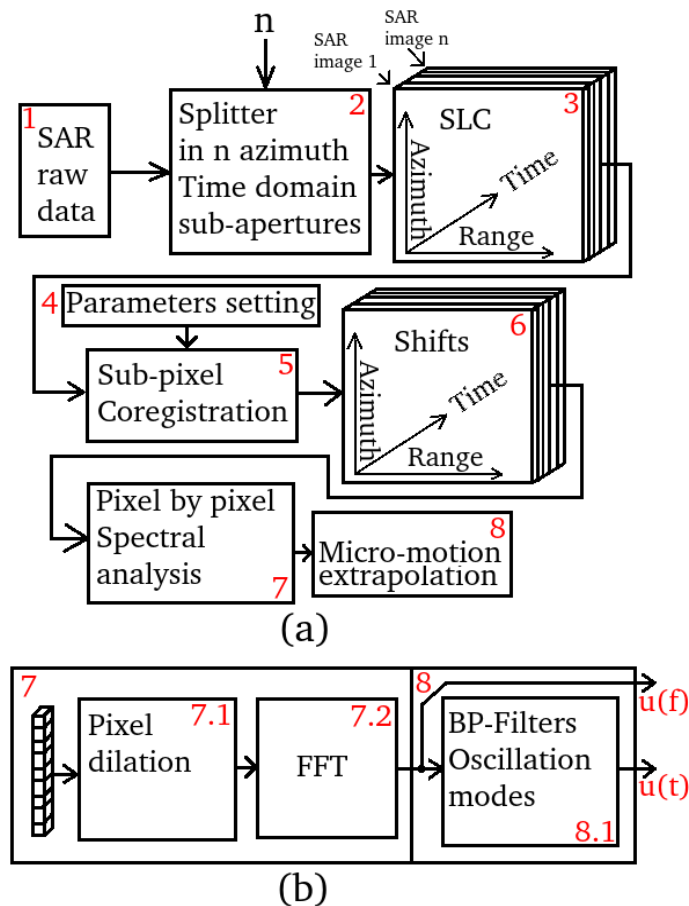


Figure 1. Computational architecture scheme. (a): General scheme. (b): Detailed scheme concerning computational blocks 7 and 8.

- 274 15. Giles, A. B., R. A. Massom, and R. C. Warner. "A method for sub-pixel scale feature-tracking using Radarsat
 275 images applied to the Mertz Glacier Tongue, East Antarctica." *Remote Sensing of Environment* 113.8 (2009):
 276 1691-1699.
- 277 16. Wang, Zhiying, Daniele Perissin, and Hui Lin. "Subway tunnels identification through Cosmo-SkyMed
 278 PSInSAR analysis in Shanghai." 2011 IEEE International Geoscience and Remote Sensing Symposium.
 279 IEEE, 2011.
- 280 17. Perissin, Daniele, and Teng Wang. "Repeat-pass SAR interferometry with partially coherent targets." *IEEE
 281 Transactions on Geoscience and Remote Sensing* 50.1 (2012): 271-280.
- 282 18. Nitti, Davide Oscar, et al. "Impact of DEM-assisted coregistration on high-resolution SAR interferometry."
 283 *IEEE Transactions on Geoscience and Remote Sensing* 49.3 (2011): 1127-1143.
- 284 19. Biondi, Filippo, Carmine Clemente, and Danilo Orlando. "An atmospheric phase screen estimation
 285 strategy based on multi-chromatic analysis for differential interferometric synthetic aperture radar." *IEEE
 286 Transactions on Geoscience and Remote Sensing* (2019).

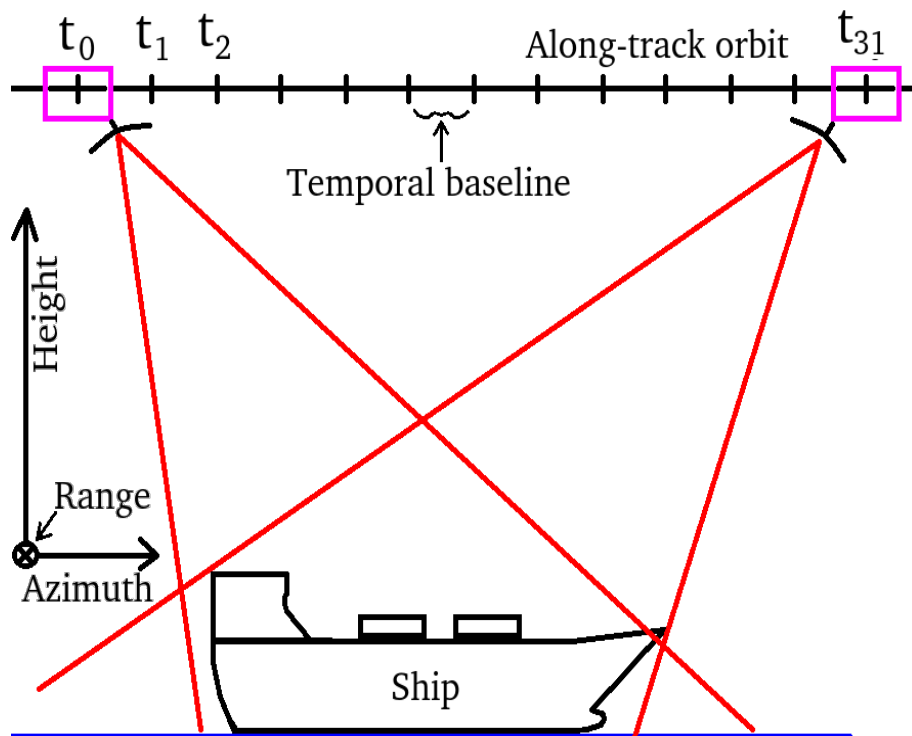


Figure 2. SAR geometry of the small multi-temporal baseline strategy.

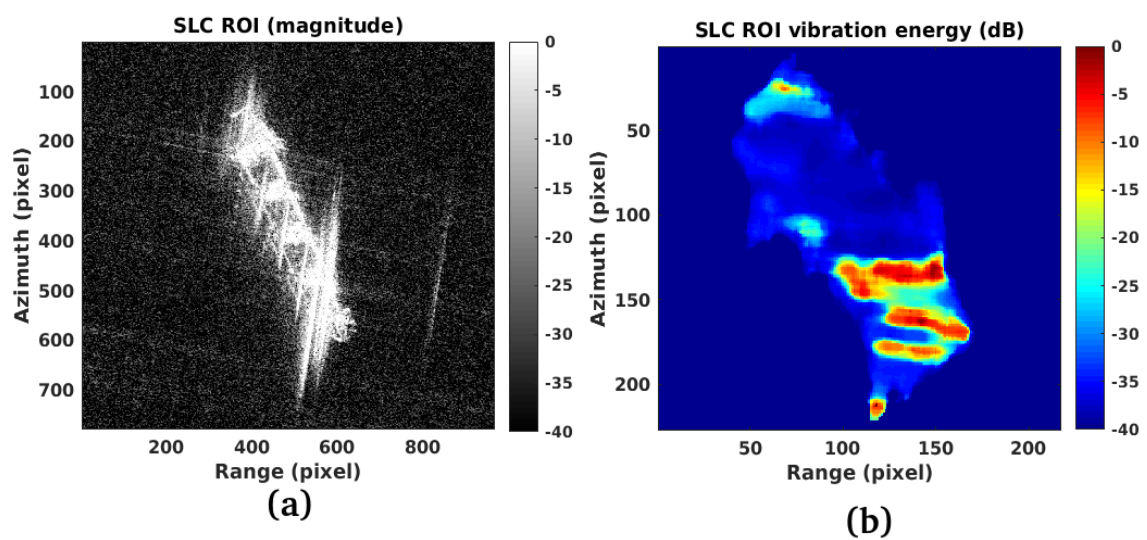


Figure 3. (a): SLC of the ROI under test. (b): Vibration field (magnitude).

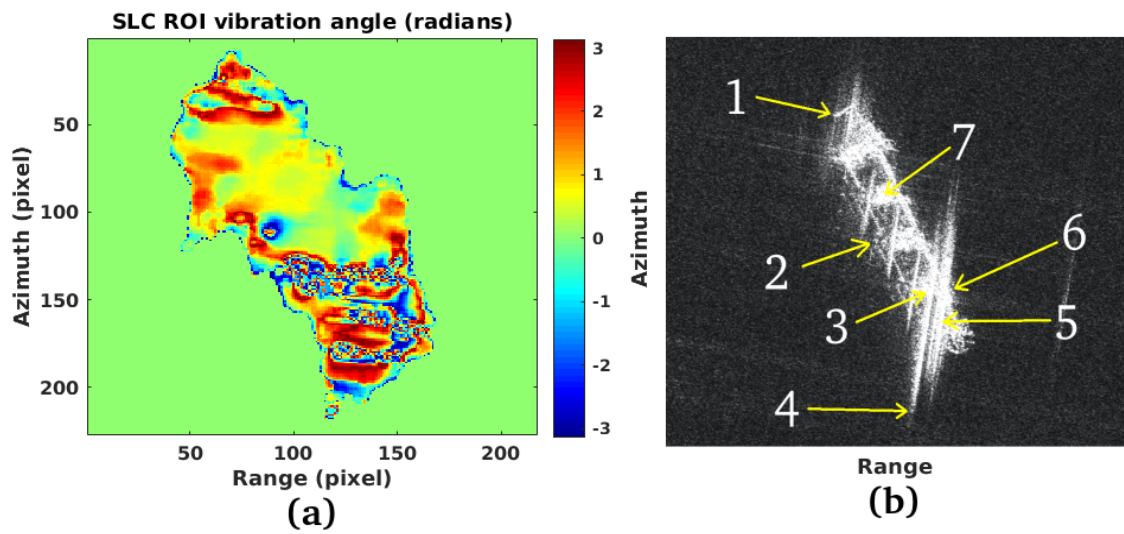


Figure 4. (a): Vibration field (phase). (b): Points of measurement representation.

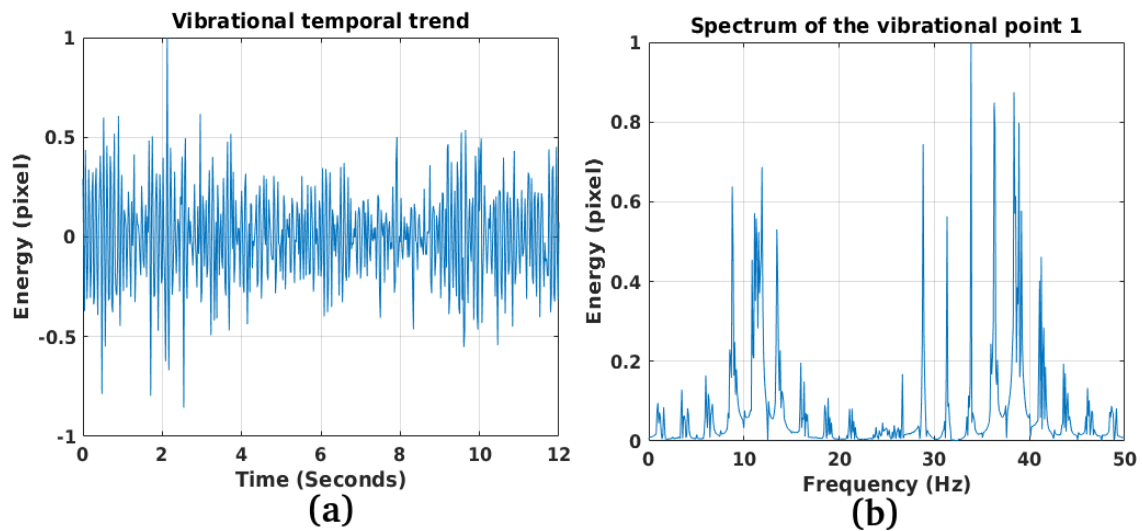


Figure 5. (a): Measurement point number one temporal trend. (b): Measurement point number one frequency spectrum.

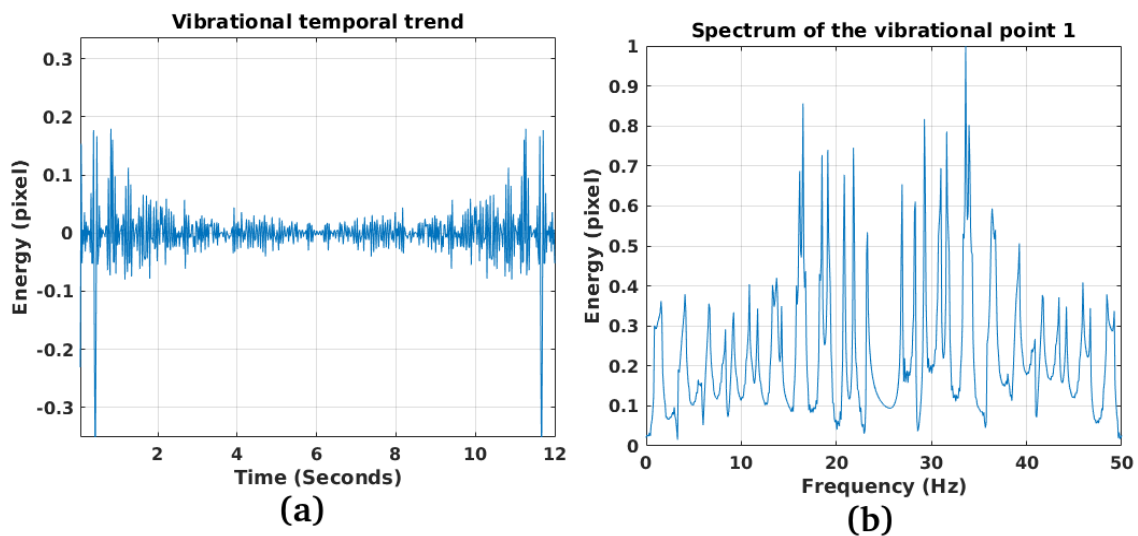


Figure 6. (a): Measurement point number two temporal trend. (b): Measurement point number two frequency spectrum.

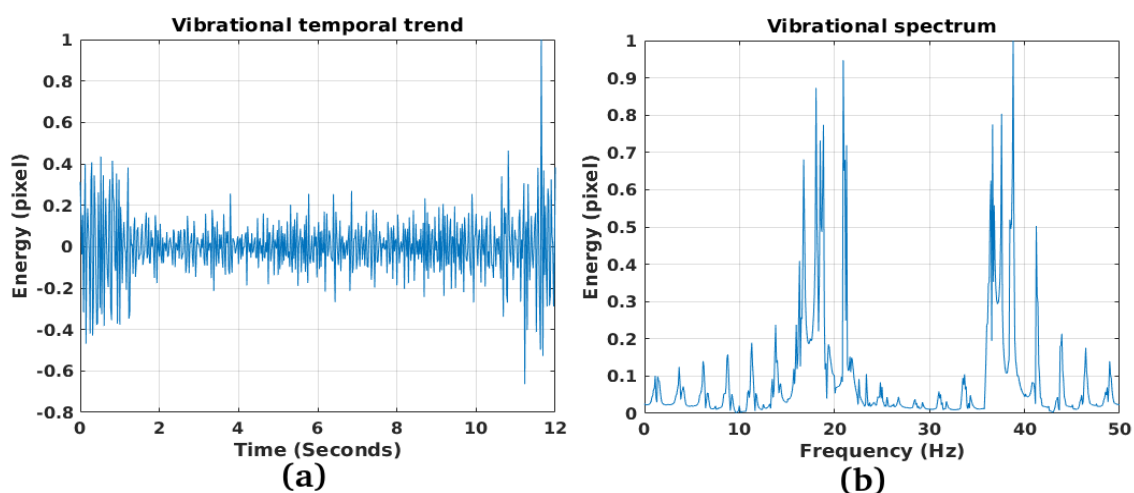


Figure 7. (a):Measurement point number three temporal trend. (b):Measurement point number three frequency spectrum.

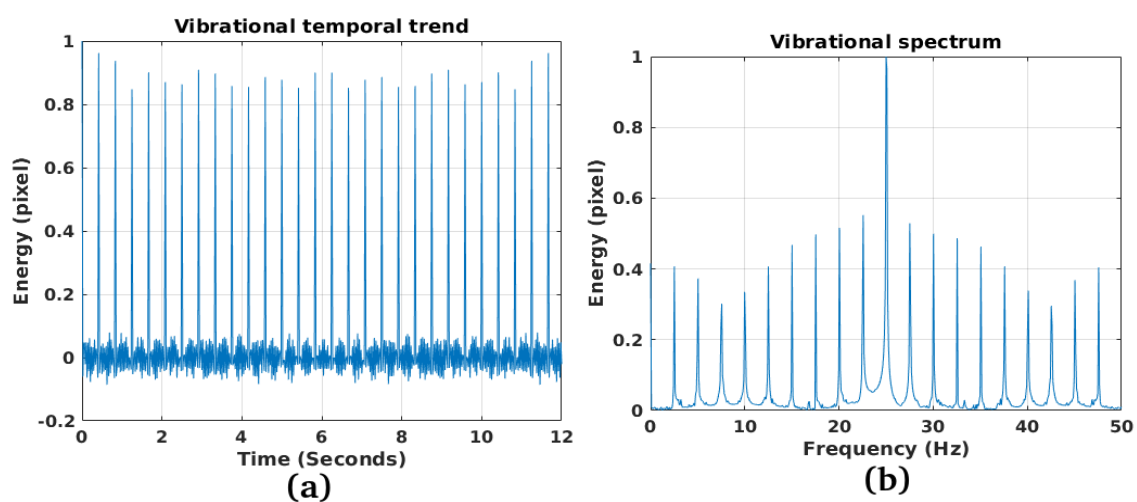


Figure 8. (a):Measurement point number four temporal trend. (b):Measurement point number four frequency spectrum.

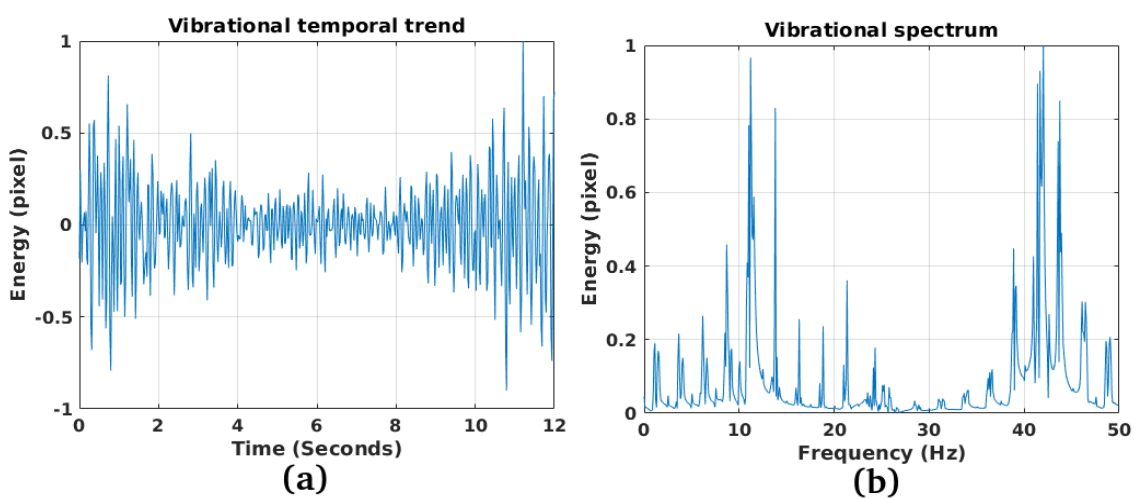


Figure 9. (a):Measurement point number five temporal trend. (b):Measurement point number five frequency spectrum.

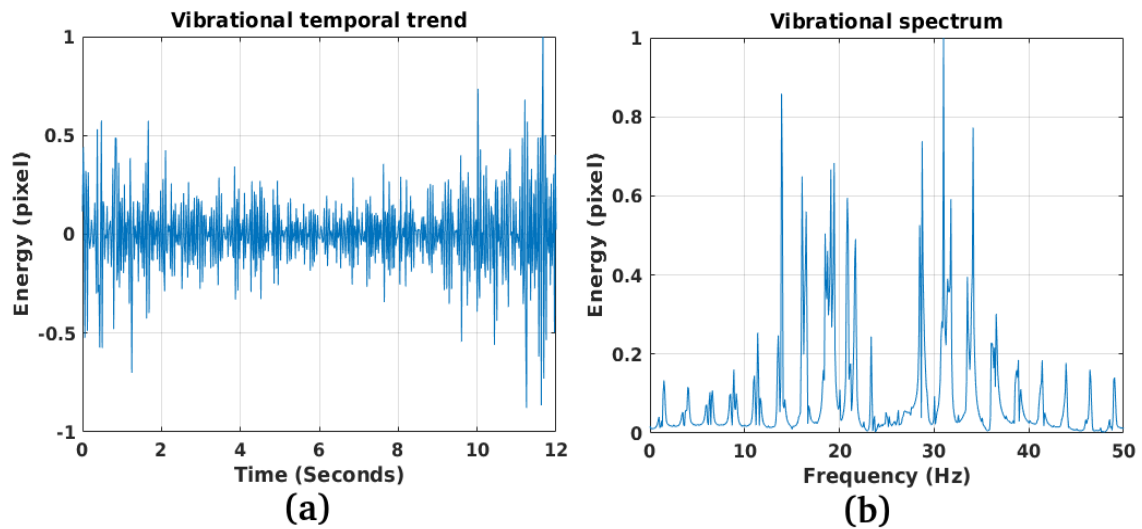


Figure 10. (a):Measurement point number six temporal trend. (b):Measurement point number six frequency spectrum.

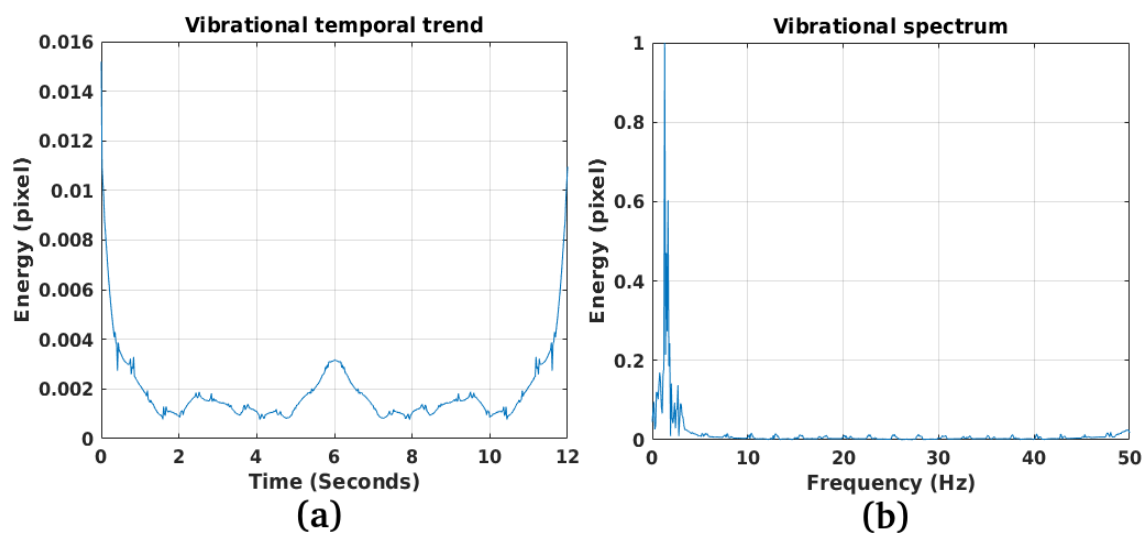


Figure 11. (a):Measurement point number seven temporal trend. (b):Measurement point number seven frequency spectrum.

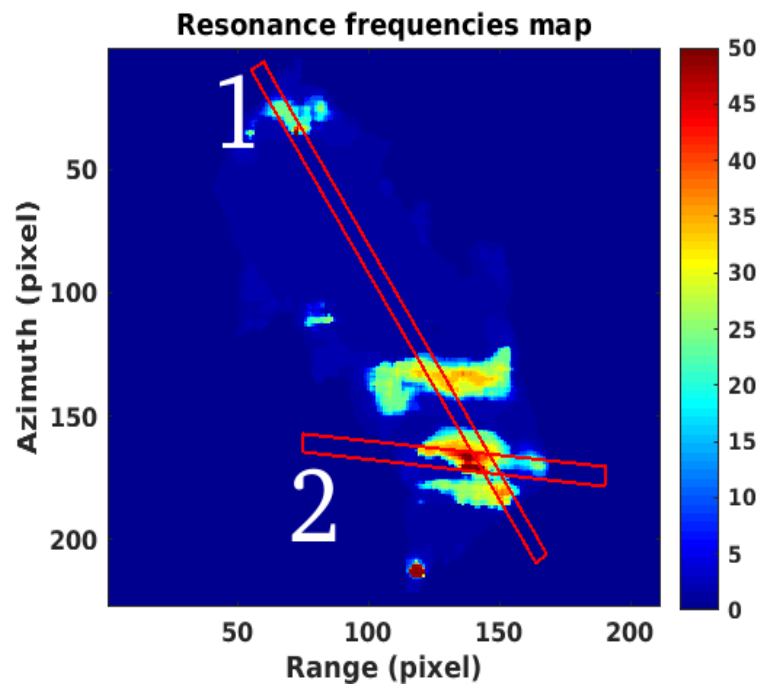


Figure 12. Vibrational profiles selected for results discussion.

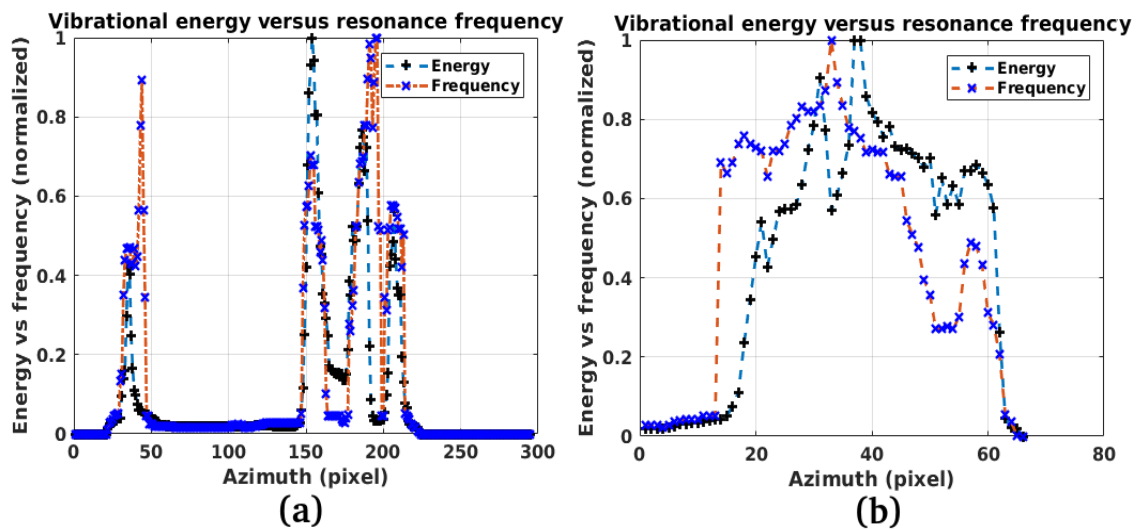


Figure 13. Vibrations observed along the profiles selected in Figure 12. (a): Vibrational profile 1. (b): vibrational profile 2.

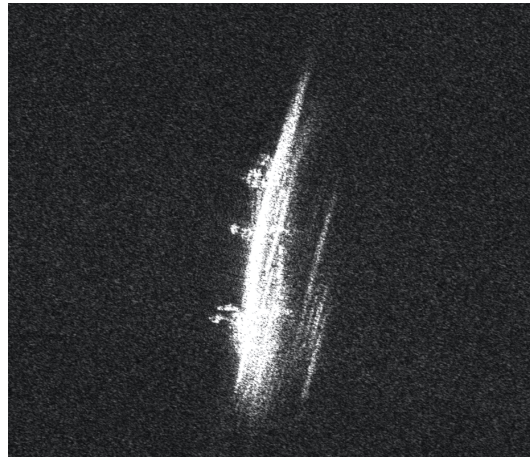


Figure 14. S11 polarimetric channel SLC SAR of the study-case number two river.

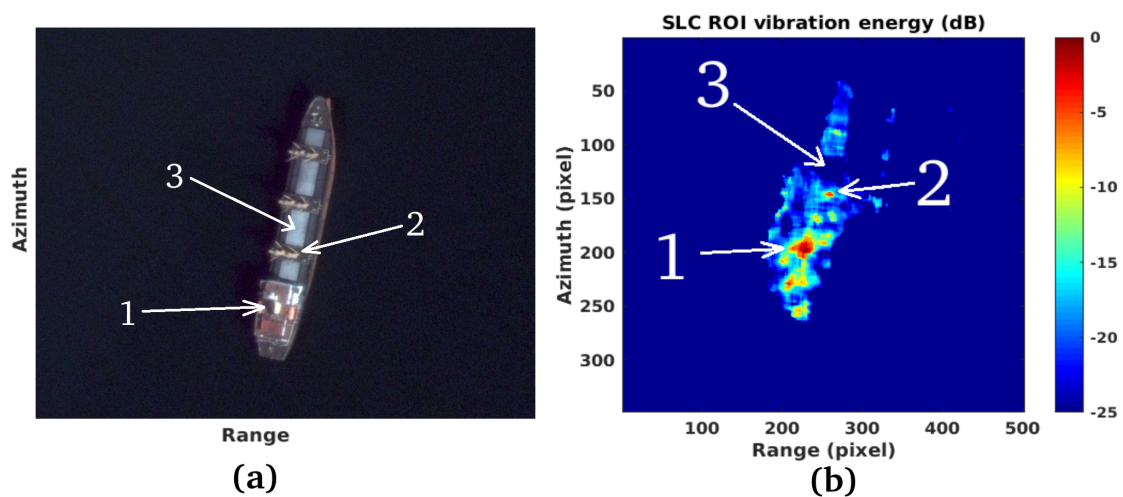


Figure 15. S11 polarimetric channel SLC SAR of the study-case number two river.

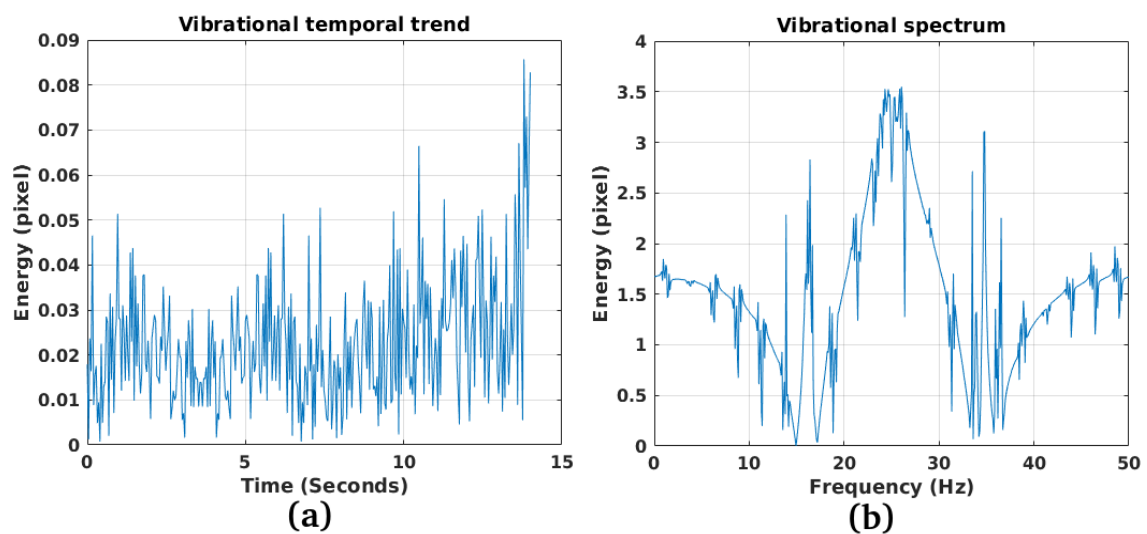


Figure 16. S11 polarimetric channel SLC SAR of the study-case number two river.

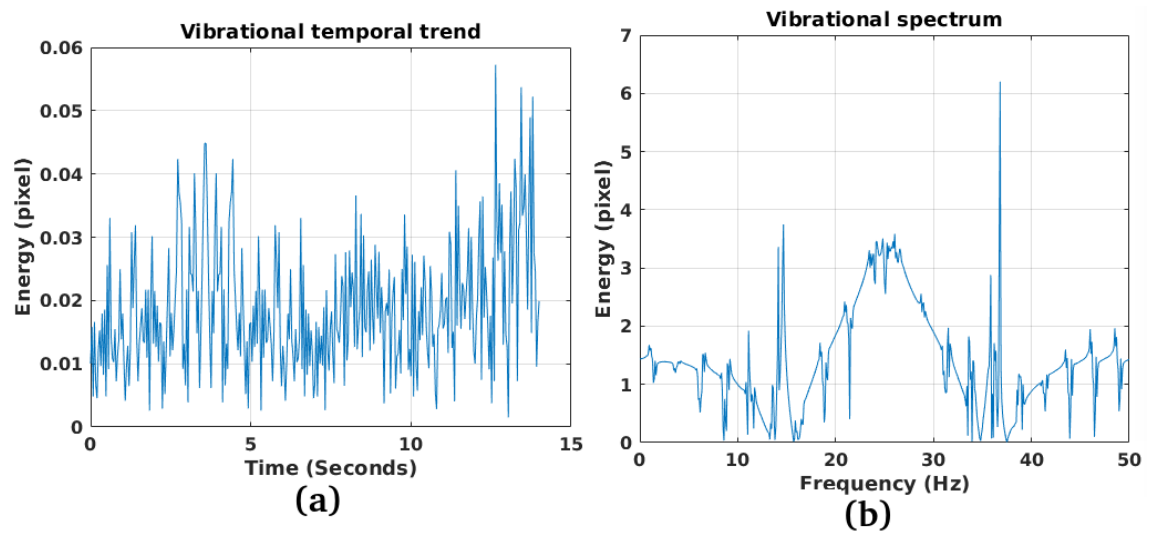


Figure 17. S11 polarimetric channel SLC SAR of the study-case number two river.